

# Evaluation and Optimization of a Multi-component Planar Doppler Velocimetry System

Gregory S. Elliott\*

*University of Illinois Urbana-Champaign, Urbana, Illinois, 61801*

Jim Crafton†

*Innovative Scientific Solutions Inc., Dayton, Ohio, 45440*

*and*

Henry D. Baust‡, Thomas J. Beutner§, Campbell D. Carter\*\*, Charles Tyler††  
*Air Force Research Laboratory, Wright-Patterson AFB, Ohio, 45433*

A Planar Doppler Velocimetry system has been developed for multi-component velocity measurements in large scale subsonic wind tunnel facilities. System components, methodologies and improvements are evaluated and discussed. Data is presented on two component measurements conducted in the flow field above a 70 degree delta wing at an angle of attack of 23 degrees in a Mach 0.2 (69 m/s) free stream. Although only two components of velocity could be resolved, axial and spanwise measurements were made characterizing the velocity field associated with the vortex cores as they developed downstream. Detector placement and system performance was improved in a second test to measure the three dimensional velocity field above a Boeing UCAV model again at 20 degrees angle of attack operated in a Mach 0.2 free stream. The evolution of the three dimensional velocity field created by vortices from the sharp leading edge of the body and the outboard vortex above the wing was characterized. Further optimization of the current system indicated that current levels of uncertainty can be improved by proper camera placement to reduce the sensitivity to laser frequency fluctuations and by improving the linear independence of the measured velocity components as characterized by the condition number of the coefficient matrix. Other considerations of camera placement and considerations to make measurements are also discussed.

## I. Introduction

MOLECULAR/ATOMIC filter techniques offer the potential of quantitative, multi-component, velocity measurements in a plane and appear well suited to applications in large-scale facilities. Over the last fifteen years a variety of research groups have developed and utilized molecular-filter-based techniques to measure velocity. These include Planar Doppler Velocimetry (PDV<sup>1,2,3,4,5</sup>) Doppler Global Velocimetry (DGV<sup>6,7,8,9,10</sup>), Filtered Planar Velocimetry<sup>11,12</sup> Absorption Filter-Planar Doppler Velocimetry,<sup>13</sup> and Filtered Rayleigh Scattering (FRS) Velocimetry<sup>14</sup>. In addition, molecular-filter-based methodologies have been investigated utilizing scattering from molecules to obtain property measurements other than velocity.<sup>15,16,17,18</sup> It should be recognized that the early work of Komine and Brosnan,<sup>6</sup> Komine et al.,<sup>19</sup> and Meyers and Komine<sup>20</sup>, who introduced molecular filters to aerodynamic measurement, pioneered several of the features common to many molecular-filter-based diagnostics.

---

\* Associate Professor, Aerospace Engineering, 104 South Wright St., Associate Fellow.

† Engineer, 2766 Indian Ripple Rd., Member AIAA.

‡ Project Engineer, AFRL/VAAI, 2145 Fifth St., Member AIAA.

§ Program Manager, AFOSR, 4015 Wilson Blvd., Arlington, VA 22203, Associate Fellow.

\*\* Senior Aerospace Engineer, AFRL/PRA, 1950 Fifth Street, Associate Fellow.

†† Aerospace Engineer, AFRL/VAAC, 2210 Eight Street, Bldg 146, Rm 225, Associate Fellow.

Their work outlined many of the basic ideas of DGV (and PDV) and stand as the original proofs-of-concept for the data collection and analysis methodologies that are summarized in recent review articles.<sup>5,21, 22</sup>

PDV has distinct attributes that make it an attractive velocimetry technique for some applications. The PDV technique does not require resolution or tracking of individual particles in the flow. In fact, the PDV technique lends itself well to particle-laden flows, such as flows with natural condensation. The PDV technique integrates the intensity of all scattering in the location corresponding to the probe volume. Because PDV does not require individual particles to be resolved in the flow, it can be used in situations where a sharp focus of the flow field is not possible. This feature is advantageous in many wind tunnel applications where limited optical access may result in distorted viewing angles. PDV is also tolerant of high through-plane velocities, and may therefore be used in highly three-dimensional flows. PDV is also based on a single laser pulse interrogation of the flow. No double exposures are required, so the technique may be used to resolve transient events. The PDV technique allows three-component velocity data to be collected over an entire plane in a flowfield during the duration of a single laser pulse.

However, PDV also presents several challenges to the experimentalist. The basis of the PDV technique requires spectral frequency shifts to be resolved through intensity-based measurements. Thus, any aspect of the experiment that corrupts either the frequency measurement, or the intensity field, may result in an error in the data, including laser speckle, background light, temperature sensitivities of filters, acoustic and vibration excitation of the laser, laser reflections, etc. Measurement of multiple velocity components requires either multiple camera systems or multiple illumination directions—in either case necessitating optical access from multiple angles in the wind tunnel. The intensity of the light used to measure the Doppler shifts depends on both laser intensity as well as seeding density in the wind tunnel test section, both of which pose challenges for implementation in wind tunnels. High power laser beams, particularly when formed into laser sheets, may damage windows or model surfaces, and seeding large areas of the wind tunnel with fog, smoke, or other seed material may be difficult. Some of these are practical concerns associated with the test environment, others are specific error sources that have been addressed in the development of the PDV system and will be discussed in more detail below.

Molecular-filter-based velocimetry techniques are based on measuring the Doppler shift of laser light scattered off of moving particles. These particles are often seeded into the flow (such as smoke, fog, aluminum oxide, etc.) or may occur naturally through condensation processes. When the laser light is scattered by a moving particle, the frequency of the light is shifted according to the Doppler shift equation:

$$\Delta f_D = \frac{1}{\lambda} (\underline{k}_o - \underline{k}_i) \cdot \underline{V} \quad (1)$$

where  $\Delta f_D$  is the Doppler shift,  $\lambda$  is the wavelength of the incident laser light,  $\underline{k}_o$  is the unit vector in the scattering direction (sometimes referred to as the observation vector),  $\underline{k}_i$  is the unit vector in the direction of the incident laser propagation (sometimes referred to as the incident light vector), and  $\underline{V}$  is the velocity vector associated with the scattering particle. It is this Doppler shift that is measured by the molecular-filter-based diagnostic techniques described below and the determination of velocity is dependent on both accurate determination of the Doppler shift as well as the geometry of the illumination and data collection systems, which determine the unit vector directions in Equation 1. It should also be noted that the incident and observation direction vectors in Equation 1 are unit vectors, but that their difference,  $(\underline{k}_o - \underline{k}_i)$  may have magnitude from 0 to 2, affecting the sensitivity of the system.

PDV uses a narrow-linewidth laser to illuminate a plane of the flow field. This plane is then imaged by two cameras. One camera, referred to as the signal camera, views the illuminated plane through a molecular filter, to produce a “signal image”, and a second camera, referred to as the reference camera, views the plane directly (i.e. without a molecular filter), to produce a reference image. The molecular filter produces a signal image in which the intensity is dependent on the frequency of the imaged light. The pixels of the signal camera CCD array record the integrated spectral intensity that is transmitted through the molecular filter’s absorption profile and is given by  $S_{C1}$  (with the limits on the integration dependent on the spectral sensitivity of the camera and optics). The reference image records the same field of view, but without the frequency-based filtering, and is used to correct for intensity variations across the image due to seeding variations and laser intensity variations. The reference camera records  $S_{C2}$ , which is the integrated spectral intensity of the unfiltered light.

The molecular filter is simply an optical cell (a glass cylinder with windows on each end) containing a molecule having an absorption line in the frequency tuning range of the illuminating laser. This results in a filter that has a transmission profile with finite sloping edges as shown in Figure 1a. The term  $I_v / I_0$  is the transmission ratio of the molecular filter, with  $I_v$  defined as the spectral intensity (intensity at frequency  $\nu$ ) measured after light has transmitted through the cell, and  $I_0$  defined as the spectral intensity of the light before entering the cell. As the light scattered from particles passes through the molecular filter, it is partially absorbed depending on its frequency and the absorption profile of the molecule present within the cell. As shown in Equation 1, the frequency of the scattered light is dependent on both the frequency of the laser and the change in frequency, due to the Doppler shift.

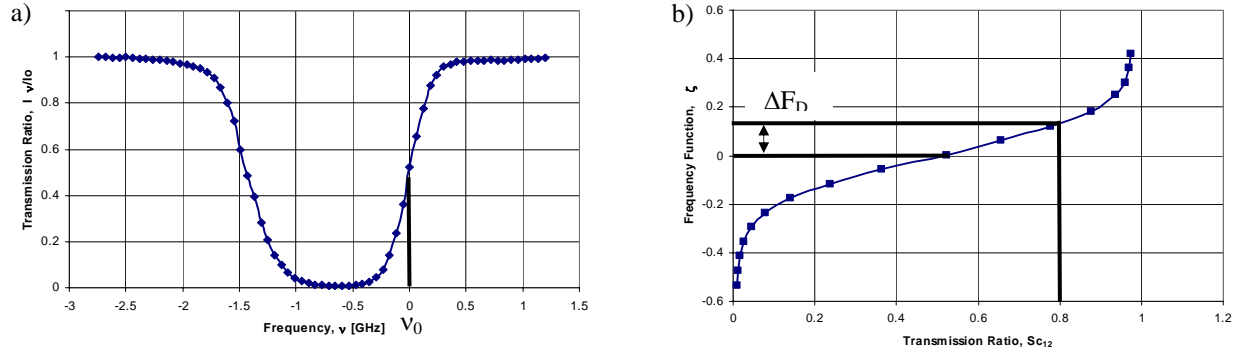


Figure 1. Schematic of intensity spectra of PDV process showing the (a) transmission profile of the iodine filter, and resulting frequency function (b).

Therefore, with the laser tuned to a point with partial transmission (i.e. at 0 GHz in Figure 1a), the transmission of imaged light through the filter may either increase or decrease depending on the direction of the Doppler shift (i.e. higher or lower frequency) and the nominal laser frequency.

From the cameras, the transmission ratio through the cell ( $S_{C12}$ ) is obtained by dividing the intensities of the signal ( $S_{C1}$ ) and reference ( $S_{C2}$ ) cameras at corresponding pixels after proper calibration which will be described shortly. Figure 1b shows a plot of the transmission ratio calculated from the cameras as the independent variable and the frequency shift (or frequency function) as the dependent variable. In an experiment, once the transmission ratio ( $S_{C12}$ ) at a given point in the image is known (i.e. at  $S_{C12} = 0.8$  in Figure 1b), the Doppler shift can be found using the frequency function of the filter (assuming the frequency of the laser is known). This process is repeated at each camera pixel and the velocity is then calculated at each pixel of the image using this measured Doppler shift in accordance with Equation 1. Since the measured Doppler shift is dependent on the vector difference between the illumination and observation unit vectors multi-component velocity measurements may be made—either by viewing the flow field from more than one direction (i.e. changing the direction of the observed vector), or by illuminating the flow field from multiple directions (i.e. changing the direction of the incident light wave vector). Both approaches have been used by researchers in order to make multi-component measurements.<sup>23,24</sup>

Over the past seven years we have developed molecular-filter-based velocimetry systems (including both hardware and software) and have investigated its application in various flow fields of interest in the Subsonic Aerodynamic Research Laboratory (SARL) wind tunnel facility at Wright Patterson Air Force Base.<sup>2, 24, 25</sup> This paper summarizes the discoveries that have been made in the development of a three component PDV system utilized to study the velocity fields in the SARL wind tunnel. First the PDV system will be described highlighting equipment and methodologies that were developed as part of the final system. Next we will describe the procedure that was utilized to convert the raw images into desired velocity components. This will be followed by the presentation of example data from wind tunnel tests conducted on a delta wing and a Boeing UCAV model measuring multiple velocity components. This will be followed by a brief discussion on considerations for camera placements to reduce system uncertainties when computing multiple velocity components.

## II. PDV System

A schematic of the PDV system is shown in Figure 2. The main components are the laser and sheet forming optics, the iodine filters, the laser frequency monitoring and cell calibration system, and the receiving optics and cameras. A frequency-doubled Nd:YAG laser<sup>26</sup> was used in the current experiments. The laser was injection seeded,<sup>27</sup> operated at a repetition rate of 10 Hz with a pulse duration of about 10 ns and energy per pulse in excess of 300 mJ. With injection seeding, the laser produced a narrow linewidth pulse ( $\sim 140$  MHz) with a center frequency that could be tuned over a range of 70 GHz by applying a bias voltage to the seeder. It should be noted that because the integrated transmission through the iodine cell is measured, as noted above, it is possible to measure a Doppler shift of the laser light which is much smaller ( $\sim 3$  MHz) than the laser linewidth itself.

In order to improve the stability of the laser frequency (particularly in a noisy large wind tunnel environment) the laser was supported on actively controlled pneumatic vibration isolators. This vibration isolation was necessary since both vibrations and acoustic noise in the wind tunnel operating environment can have a detrimental effect on the ability of the laser to seed properly. Several absorption features of iodine are within the frequency tuning range

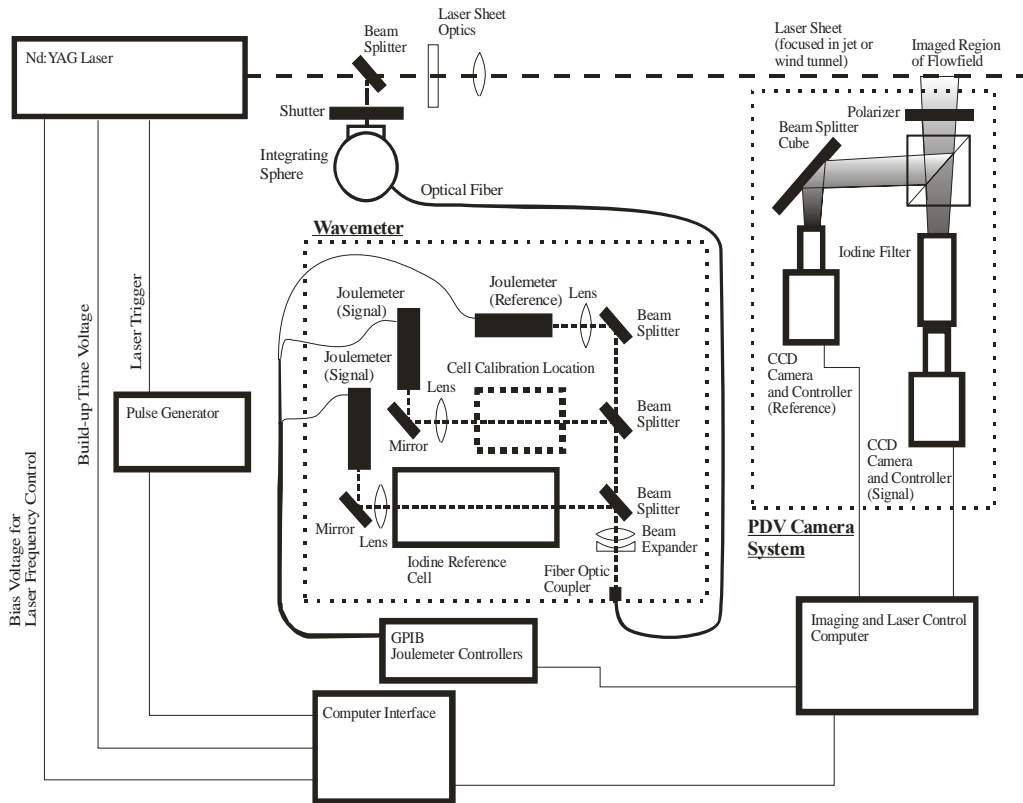


Figure 2. Planar Doppler Velocimetry experimental arrangement.

of the Nd:YAG laser and have been extensively reported elsewhere.<sup>21</sup> The absorption line used for the experiments in this study was centered at a wavenumber of  $18789.28 \text{ cm}^{-1}$ .

The laser light was formed into a thin sheet using a combination of spherical and cylindrical lenses and this sheet was projected into the wind tunnel and defined the PDV measurement plane. Although the Nd:YAG laser is a relatively stable platform, it is characterized by two features that complicate PDV implementation. First, its long term frequency drift and pulse-to-pulse fluctuations (ranging from 10 to 50 MHz depending on the acoustic and vibration environment) necessitate a frequency monitoring system (hereafter referred to as a wavemeter) to monitor the laser frequency on a pulse-by-pulse basis. This wavemeter will be described below. Second, several investigators have reported a chirp, or spatial variation in frequency, for the Nd:YAG laser of up to 150 MHz.<sup>28,29</sup> One solution to this problem is to use only the center of the laser profile which has been reported to reduce the variation to less than 4 MHz.<sup>28</sup>

One of the key elements of the PDV system addressed during the course of the development effort, was the ability to control the absorption profile of the iodine filter. The final filter design is shown in Figure 3.<sup>30</sup> The iodine filters used in the current set of experiments were generally cylindrical in shape, 8 cm in diameter, and from 12 to 25 cm in length, with flat optical plates at each end. The filters used in this study were a starved iodine filter design where only iodine in the vapor state was contained in the cell body. This arrangement ensured that no communication with solid iodine could cause the number density of the vapor to change with temperature, which results in unstable absorption profiles. The cylindrical portion of the cell was wrapped with heating tape and insulation and maintained at  $105^\circ\text{C}$  via a closed-loop temperature controller. When filling the cell, the side arm, which is connected to the body of the cell, was maintained at a lower temperature (generally  $40^\circ$  to  $50^\circ \text{C}$ ) using a constant temperature water bath. After solid-vapor equilibrium was established in the side arm, a valve on the side arm was closed shutting it off from the body of the cell and fixing the number density of the iodine in the cylindrical portion of the filter. If there was no further need to change the absorption line profile for the cell, the glass cold finger could be permanently welded shut, removing the valve and insuring that the number density of iodine in the cell would not change due to leakage of the valve. In addition to the iodine vapor, in some cells a small amount of



Figure 3. Typical iodine filter (cell) configuration [Ref. 30].

measured the transmission of a small portion of the laser light through a separate iodine filter, termed the reference filter, for each laser pulse. By monitoring the laser intensity before and after the beam went through this cell, the frequency of the laser could be calculated for each laser pulse. The initial frequency monitoring system utilized photodiodes from which the signal was integrated utilizing a boxcar integrator.<sup>31</sup> The photodiodes and boxcar integrators were later replaced by Joulemeters. When passing a collimated laser beam through the iodine cell, care must be taken not to saturate the transition lines of the iodine gas in the laser beam path. To avoid saturation, the wavemeter measurement used only a small portion of the laser beam, reflected from the first surface of an optical wedge. The laser beam was then passed into an integrating sphere as illustrated in Figure 2 so that light from the entire beam profile was averaged before being launched into an optical fiber. The optical fiber directed the beam sample to the wavemeter detection system, shown in Figure 4, where the light from the fiber was expanded and collimated to a diameter of approximately 25 mm. This allowed a substantial quantity of light to be sent through the filter without saturating the transition in the filter cell. Checks for iodine cell saturation were performed by placing a neutral density filter in the beam path both in front of and behind the iodine cell. If saturation was present, these two neutral density filter locations would result in different intensity readings for the wavemeter signal photodiode. Two successive beam splitters then split the laser light into three beams. One beam was sent through the reference filter, the second was sent through a camera filter that had been placed in the calibration position on the optical setup (during a test this filter was moved to its position in front of the camera) and the third beam provided the intensity reference for the transmission calculation. The Joulemeters not only provided temporal integration of the intensity signal, but also had an extremely low detection limit and a linear dynamic range of about five orders of magnitude. The Joulemeters were controlled through a GPIB interface which was directly connected to the GPIB card on the Master computer.

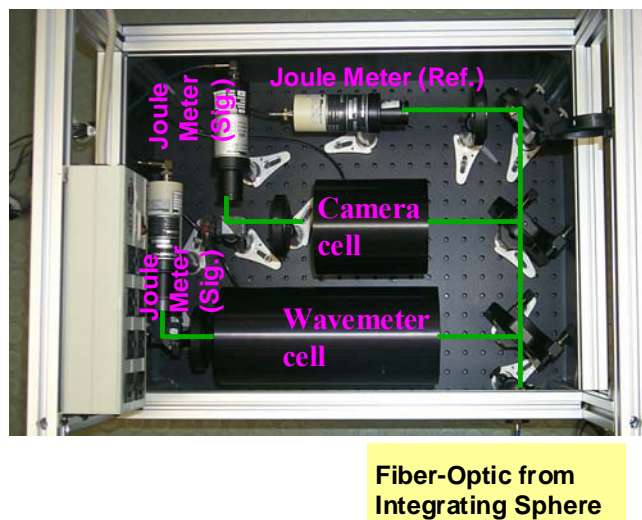


Figure 4. Final wavemeter system developed for laser frequency monitoring and iodine cell calibration.

nitrogen (~20 Torr) was added to the cell to pressure broaden the transmission profile of the cell and increase the range of measurable frequency shifts. The variation of the transmission profile to partial pressure of nitrogen, filter sidearm temperature, and filter cell temperature has been reported previously.<sup>2</sup>

A laser frequency monitoring system, or wavemeter, was developed to monitor the jitter and drift in the Nd:YAG laser about its set point and calibrate the various iodine filters used in multi-component experiments. The wavemeter

Three PDV camera systems were packaged as shown in Figure 5 so that they could be moved to the various viewing angles used for each test. Each system consisted of a polarizer followed by a 7.6x7.6 cm nonpolarizing cube beam splitter providing separate optical paths to two 16-bit back-illuminated CCD cameras with a 512 by 512 pixel array.<sup>32</sup> These cameras were generally fitted with either 85mm or 105 mm fixed focal length lenses. The f-number of the lens was set as low as possible to reduce laser speckle, but high enough to keep the entire field of view in focus (indicated  $f\# = 2.8$  to 5.6). The polarizer was used to reduce polarization-dependent variations that might occur in the scattering process in the flow field and through the Plexiglas windows and other optical components. The signal camera viewed the flow through a molecular iodine filter and the reference camera viewed the flow without a filter. A 10 cm diameter flat mirror ( $\lambda/4$ ) was used to orient the image onto

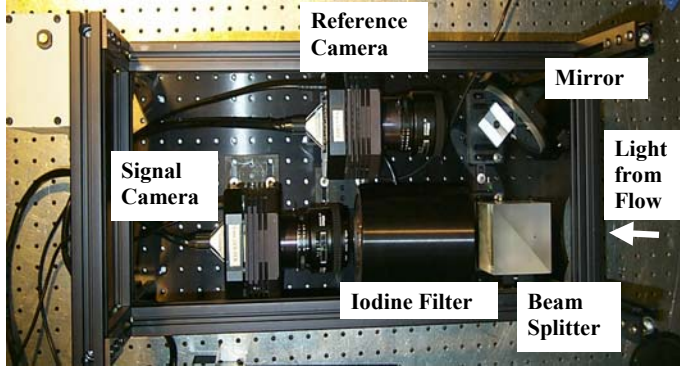


Figure 5. PDV camera system.

the reference camera and allow for both signal and reference optical path lengths to be approximately equal. A 20.4 cm starved iodine cell was placed in front of the signal camera for all PDV components. Neutral density filters were placed in front of each reference camera so that it had approximately the same intensity as the signal camera. This insured that the reference camera did not saturate while the signal camera was still at a low intensity. High and low pass optical color glass filters were also placed in front of each camera lens (creating a broadband notch filter) to reduce the intensity contribution of background ambient light.

Each of the PDV reference and signal camera systems were controlled by a single computer. Two of the computers operated as slaves and were networked into the third computer that operated as the Master for timing and synchronization of all data collection processes. For the multiple component tests, the Master computer not only controlled the slave systems but also collected and stored all the images (reference and signal) from each sub-system. The Master computer also collected laser frequency data from the wavemeter and controlled the bias voltage supplied to the laser seeder, thus controlling the laser frequency. A logfile for each test recorded file names, laser operating conditions, and user defined inputs describing the test conditions.

### III. Data Collection Methodology

Before collecting the actual PDV images a significant system calibration process had to be undertaken. The calibration included three types of data: 1) iodine cell transmission functions, 2) simultaneous spatial calibration of all cameras (also termed image mapping) and 3) intensity calibration of the signal and reference cameras. Following is a description of how the data for these calibrations were obtained as well as general recommendations for PDV data collection procedures.

Multiple iodine cells are needed in the current PDV system, one in front of each signal camera and one in front of the signal photodiode of the wavemeter system. The cell conditions (sidearm temperature, body temperature, and partial pressure of buffer gas) influence the transmission profile and were set according to the expected velocity ranges for a test. Before flow field measurements were made, all cells were calibrated using the system seen in Figures 2 and 4. Calibration consisted of scanning the laser frequency (by applying a bias voltage) while measuring the transmission profile of the iodine cells using the photodiodes connected to boxcar integrators or Joule-meters. Absolute frequencies could be obtained for the transmission profile by comparison with multiple absorption peaks in a known model of the iodine absorption spectrum (as provided by Forkey et al<sup>29</sup>), utilizing a Fabry-Perot etalon, or imaging a reference velocity field, such as a rotating wheel. Figure 6 shows an example of the filter scans taken for the four iodine cells used in the delta wing test to be presented here as well as the model spectrum. As can be seen, slight variations are present in each transmission profile due to differences in the number density of iodine or nitrogen in the cell, thus each cell must be individually calibrated. It is also important to note that the transmission profile shown in Figure 6 is the result of a finite linewidth laser transmission through the cell. Since the linewidth of individual lasers may vary, the cells must be calibrated with the laser to be used in the test. The absorption line utilized in the present experiments is located at a wavenumber of approximately  $18789.28 \text{ cm}^{-1}$ .

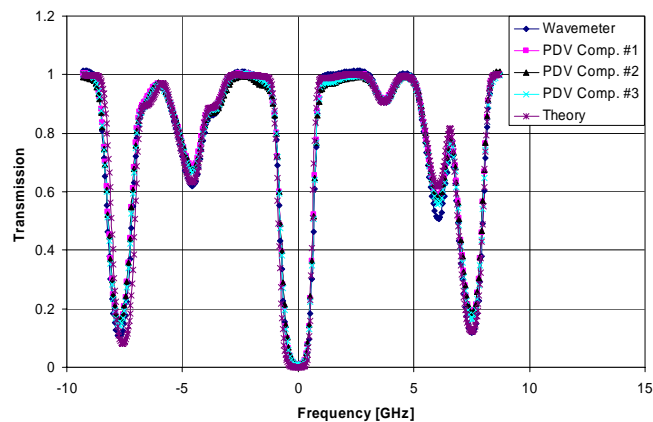


Figure 6. Comparison of theoretical and measured iodine absorption lines relative to the absorption feature at  $18789.28 \text{ cm}^{-1}$ .

from the transmission ratios measured by the wavemeter and cameras. Utilizing the appropriate frequency function ( $\zeta$ ), the frequencies measured as a function of the transmission ratio through the iodine cell (S) are denoted  $\zeta_{c1}$  ( $S_{c12}$ ),  $\zeta_{c2}$  ( $S_{c34}$ ),  $\zeta_{c3}$  ( $S_{c56}$ ) and  $\zeta_r$  ( $S_r$ ) for the three PDV camera components and the wavemeter, respectively.

In order to make accurate PDV measurements, images are needed to calibrate the camera images spatially. Dot card images were used to provide a spatial reference for each of the six cameras. The physical dot card with equally-spaced circular or rectangle dots was placed at the location of the light sheet so that optical distortions associated with the optical path differences and the oblique viewing angles could be measured. Ideally, the dots should be large enough so that they take up several pixels (8-16) and spaced far enough apart so that the centroids can be determined without interference from neighboring dots (a systematic study of the effect of dot diameter is described by Crafton et al.<sup>24</sup>). The dot card data could then be used to map the distorted camera images to a Cartesian plane corresponding to the physical dot card location. This process was critical not only to allow velocity measurements from the three camera systems to be referenced to a corresponding physical location, but also to allow for slight misalignments or magnification differences between the signal and reference images in each camera component to be accounted for.

Another calibration data set was taken to normalize the intensity of the signal and reference cameras (sometimes termed white card images or green card images, depending on the illumination source). When taking these intensity calibration shots the laser is tuned to a region of the iodine absorption profile for which the transmission is near a maximum and shows little dependence on frequency. While white light could be used, laser light was preferred because due to slight chromatic differences in the signal and reference optical paths when using white light. There are at least three techniques for taking flat field correction data, each with distinct advantages and disadvantages:

1. Static Green Card: To obtain typical static green card data the laser is expanded diffusely to illuminate a white card or a translucent sheet. The goal is to provide as even an illumination as possible to all camera views. The intensity recorded by the camera is varied by changing to intensity of the laser using neutral density filters or increasing the exposure time on the camera to capture more laser pulses in a single frame.

2. Running Green Card Empty Tunnel: Another method of providing intensity calibration images is to remove the model or move the model to a position out of the field of view and with minimal aerodynamic loading, and obtain images of the laser sheet illuminating the seed particles with the laser tuned away from the absorption line in a flat portion of the filter profile as described before. The advantage of this method is that it can be conducted during the wind tunnel test and the scattering is the same as will be seen in the measurement. Care must be taken, however, to insure that the Doppler shift caused by the flow does not shift the frequency of the light into the transmission profile of the iodine filter.

3. Running Green Card with Model: The final type of green card image is the running green card with model in place. This type of intensity calibration image is taken with the model in place and a seeded flow field with the laser tuned away from the absorption line. The advantage of the running green card with a model is that it is the easiest to take since it does not require the model to be removed, however, as with the Empty Tunnel green card, care must be taken so that the Doppler Shifts associated with the scattering of light around the model do not shift the light into the iodine transmission profile.

Background images were also taken at each calibration step and were subtracted from raw camera images to account for background illumination. Since the inlet and diffuser of the SARL wind tunnel were open to the atmosphere, background images were taken frequently to account for variations in background illumination due to changes in sunlight or other background conditions that could alter the background intensity in the field of view.

After the dot-card and green-card images are taken the actual PDV data was recorded. Generally the laser was tuned to approximately the 50% transmission region and the data shots were recorded. It is generally desirable to vary the laser frequency slightly within this region, particularly when multiple velocity components are measured, since one component may be tuned too far into or too far away from the absorption profile to provide useful results. In addition, background shots should be taken with the laser on and no seeding so that background illumination due to laser reflections off model surfaces and wind tunnel walls can be subtracted from the data.

The final piece of data which is needed to process PDV images into velocity components is the incident and observation unit vectors for each PDV component, as defined in Equation 1. The determination of these unit vectors requires careful measurement of the laser sheet forming optics and the camera or mirror locations for the receiving optics. Furthermore, the total path length to the cameras and the virtual origin of the light sheet must be measured to account for the varying illumination and observation directions over the field of view. This allows the incident and observation directions to be determined, and the velocity sensitivity calculated, on a pixel-by-pixel basis.

## IV. Data Processing

Not surprisingly the data processing methodologies from the various researchers of PDV are similar in their basic attributes and have been described in detail in their research articles and in review articles. The key processing steps for PDV are summarized in the schematic diagram of Figure 7 and described in detail in the following sections. After obtaining the PDV data from a test the following five image processing steps were required.

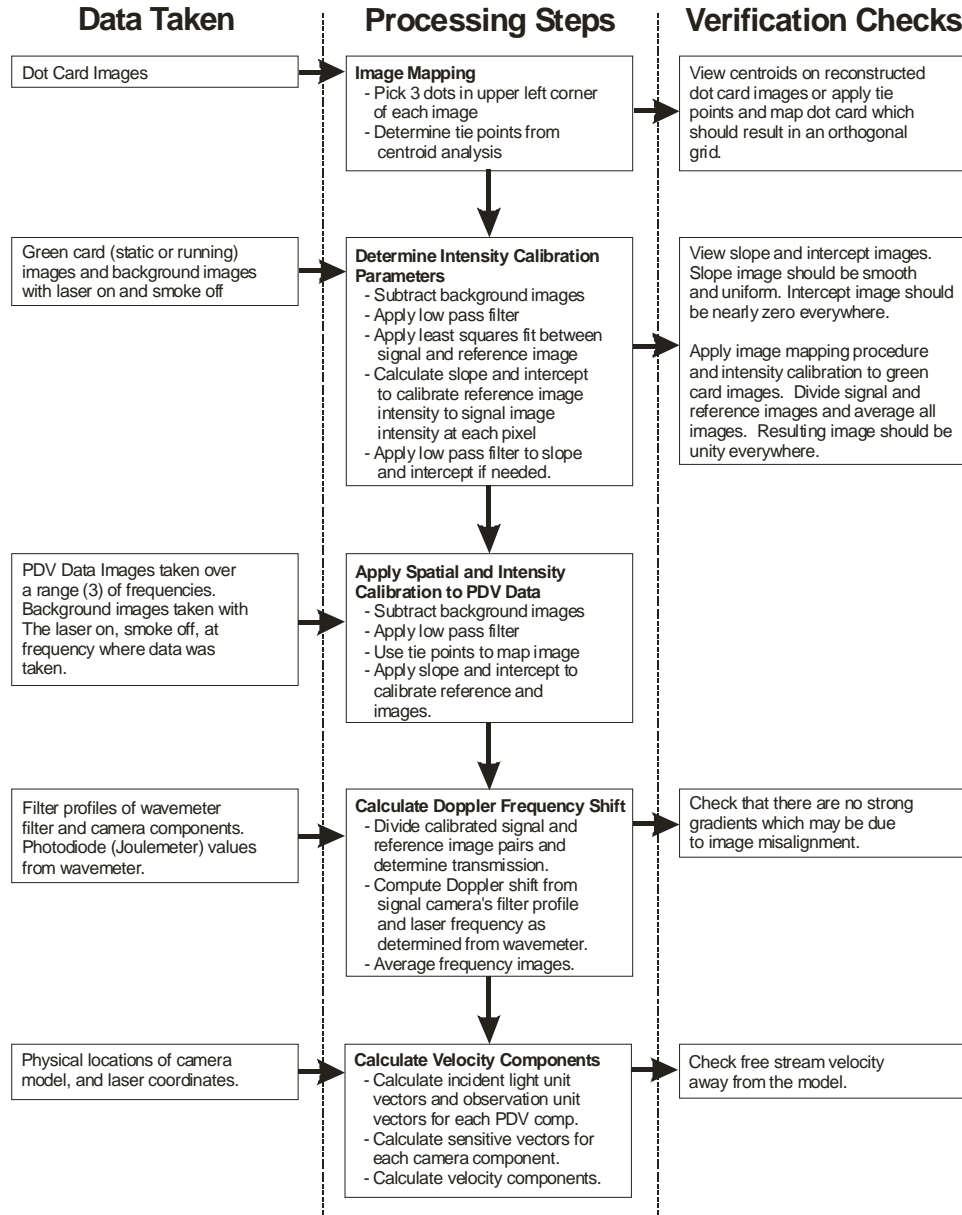


Figure 7. Diagram of main processing steps in obtaining velocity information from PDV images.

### A. Image Mapping

Signal and reference images must be aligned on a pixel-to-pixel basis in order to calculate the transmission ratio for light scattered from a given point in physical space. Both the signal and reference images were mapped to an image plane corresponding to the physical space with equally spaced pixels and all perspective distortions removed. Images of the dotcard, described previously, were used for this mapping process. A computer program found the centroid of each dot on the card in these images for all 6 cameras. These centroid locations, also referred to as tie-points, were used to provide reference points in the measured image corresponding to known mapping

points in the mapped image. For each “pixel” location in the mapped image, bilinear interpolation was used with a weighted average of the surrounding pixels in the data image to determine the appropriate pixel intensity in the mapped image. This process has been described in detail by Mosedale et al.<sup>2</sup> It should be noted that during large-scale wind tunnel tests the vibrations to the optical setup may slightly shift mirrors, beam-splitters, or cameras which are part of the PDV camera system. Therefore, dot card images were taken repeatedly throughout the test series. In addition, a spatial cross-correlation routine was sometimes required to allow for slight adjustments to the camera mapping. These corrections could be accomplished based on cross-correlations of data images or running green card images that were periodically taken during the test. If the view of the laser sheet is relatively normal and magnification of system cameras is consistent or a skewed view is acceptable the spatial cross-correlation can be utilized instead of a dotcard for image mapping.<sup>4</sup>

## B. Determination of Intensity Calibration Parameters

In addition to the mapping procedure described above, an intensity calibration procedure was required before calculating the ratio of the signal to reference images. The intensity calibration procedure accounts for intensity differences arising from the beam splitter efficiencies, additional optical components, and camera sensitivities so that the ratios recorded by the PDV camera system corresponded to the transmission ratio axis of the camera frequency function,  $\zeta_c$  determined previously.

Calibration coefficients were determined from the green card (or running green card) images described previously using a least squares methodology the slope and intercept calibration parameters were found for each pixel location. Regardless of the details of the green card acquisition, after background subtraction these images were smoothed (i.e 7x7 low pass filter for the delta wing data taken using the full camera resolution, and 5x5 low pass filter for the UCAV data that was from images where the pixels were binned by 2), mapped according to the procedure described above so that the signal and reference images ( $S_{c1}$  and  $S_{c2}$ , respectively) corresponded on a pixel to pixel basis. In addition low and high signal level thresholds were set so to avoid using camera data close to saturation or camera data with too low of a signal level, both of which will result in unacceptable errors in the processed data. Pixels exceeding these limits were marked as bad, and not used in any further processing steps. Similarly, pixels with a transmission ratio that was within 15 percent of the top of bottom of the transmission profile were also marked as bad, since the roll-off of the transmission profile at both extremes makes the errors associated with transmission in these areas unacceptable. These thresholds were initially set manually although later results (Boeing UCAV data) utilized a threshold based on rejecting any pixels that exceeded a multiple of the standard deviation from all the intensity data collected, thereby avoiding intensity outliers. Comparing various green card methodologies there appeared less deviation between the raw and calibrated intensities using the static green card, although all methods resulted in approximately the same values for the calibration coefficients. More detailed comparisons of alternative calibration procedures may be found in the final report.<sup>33</sup>

## C. Apply Spatial and Intensity Calibrations to PDV Data

After subtracting background intensity levels, low-pass filtering the images, and mapping the signal and reference images to a common image plane, the signal images were divided by the reference images on a pixel-by-pixel basis, producing a series of images containing the transmission ratio at each pixel for each of the three PDV components (i.e.  $S_{c12}$ ,  $S_{c34}$ ,  $S_{c56}$ ).

## D. Calculate Doppler Frequency Shift

The transmission ratio images were then converted to frequency through the frequency function,  $\zeta_c$ , determined during calibration procedures for each camera’s iodine cell filter. The wavemeter also recorded similar transmission data with a separate iodine cell filter, so that the frequency of each laser pulse corresponding to a PDV image could be determined. The Doppler shift was then determined for each pixel location as the difference between the measured frequency in the camera system and the nominal laser frequency measured by the wavemeter for that laser pulse:

$$\Delta f_{Dn} = [\zeta_{cn}(S_{cn}) - \zeta_r(S_r)] \quad (2)$$

where n denotes the quantity for the PDV camera component being measured, and r indicates the wavemeter measurement of the laser frequency.

## E. Calculate Velocity Components

The final step in processing PDV images was to determine the velocity from the Doppler shifts calculated at each pixel location. For simplicity we begin by rewriting Equation 1 as

$$\Delta f_{Dn} = \frac{1}{\lambda} (\underline{k}_{oin}) \cdot \underline{V} \quad (3)$$

where  $\underline{k}_{oin}$  is termed the system sensitivity vector and is the difference between the observation and incident light vectors ( $\underline{k}_o - \underline{k}_i$ ). This sensitivity vector is different for each camera view, and, in addition, it will vary slightly over the camera image, since both the incident and observation vectors vary direction over the field of view of the camera. For the results presented here the variation of vector direction in the image was not included in the analysis, but is currently being included to resolve these effects.

For every pixel in the mapped image, each of the three camera systems measured a velocity component with different  $\underline{k}_{oi}$  vectors. Writing equations for the three measured velocity components where subscripts 1, 2, and 3 refer to the three camera systems:

$$\begin{aligned} \Delta f_{D1} &= \frac{1}{\lambda} (\underline{k}_{oi1}) \cdot \underline{V} \\ \Delta f_{D2} &= \frac{1}{\lambda} (\underline{k}_{oi2}) \cdot \underline{V} \\ \Delta f_{D3} &= \frac{1}{\lambda} (\underline{k}_{oi3}) \cdot \underline{V} \end{aligned} \quad (4)$$

Similar to the single component case the Doppler shift was measured from the transmission ratio of each reference and signal camera at each location and the frequency determined from the wavemeter. This can be expressed as three equations given as

$$\begin{aligned} \Delta f_{D1} &= [\zeta_{c1}(S_{c12}) - \zeta_r(S_r)] \\ \Delta f_{D2} &= [\zeta_{c2}(S_{c34}) - \zeta_r(S_r)] \\ \Delta f_{D3} &= [\zeta_{c3}(S_{c56}) - \zeta_r(S_r)] \end{aligned} \quad (5)$$

where  $S_{c12}$ ,  $S_{c34}$ ,  $S_{c56}$  is transmission ratio determined for each of the three camera views after the mapping and calibration steps described previously, and  $\zeta_{c1}$ ,  $\zeta_{c2}$ ,  $\zeta_{c3}$  are the frequency functions of the iodine filters in front of the signal cameras in each of the three systems. Therefore the Doppler shift is measured and the sensitivity vector ( $\underline{k}_{oi1}$ ,  $\underline{k}_{oi2}$ ,  $\underline{k}_{oi3}$ ) is known from the orientation of each PDV system. Both the sensitivity vectors  $\underline{k}_{oi}$  and the unknown velocity vector  $\underline{V}$  may be written in terms of vector components and Equation 4 may be rewritten as:

$$\begin{aligned} \lambda \Delta f_{D1} &= k_{oi1x} V_x + k_{oi1y} V_y + k_{oi1z} V_z \\ \lambda \Delta f_{D2} &= k_{oi2x} V_x + k_{oi2y} V_y + k_{oi2z} V_z \\ \lambda \Delta f_{D3} &= k_{oi3x} V_x + k_{oi3y} V_y + k_{oi3z} V_z \end{aligned} \quad (6)$$

Or, in matrix form:

$$\begin{pmatrix} k_{oi1x} & k_{oi1y} & k_{oi1z} \\ k_{oi2x} & k_{oi2y} & k_{oi2z} \\ k_{oi3x} & k_{oi3y} & k_{oi3z} \end{pmatrix} \begin{pmatrix} V_x \\ V_y \\ V_z \end{pmatrix} = \lambda \begin{pmatrix} \Delta f_{D1} \\ \Delta f_{D2} \\ \Delta f_{D3} \end{pmatrix} \quad (7)$$

$$[K_{oi}] \mathbf{V} = \lambda \Delta \mathbf{f}_p$$

The velocity vector  $\mathbf{V}$ , is solved for by inverting this matrix. As will be discussed in more detail later, this matrix is solvable only if the determinate is nonzero, and the condition number of the matrix provides an indication of the linear independence of the three sensitivity vectors. In cases where a camera arrangement is used that is insensitive to one velocity component a similar 2x2 matrix may be solved for two velocity components.

## V. Results and Discussion

### A. Multiple Velocity Component Delta Wing Experiment

Figure 8 gives the camera arrangement used in the multi-component PDV test, which was conducted in the SARL wind tunnel on the 70° Delta wing model at a 23° angle of attack. Two coordinate systems are shown. First is the tunnel coordinate system (x, y, z) with the downstream direction aligned with the x axis. Second is a model-oriented coordinate system (x', y', z') with the model chord aligned with the x' axis with the model at 23° angle-of-attack. PDV data was taken at four streamwise distances. In addition, data was taken with the model removed and the model support sting was rotated and moved away from the measurement plane to provide “empty tunnel” data used to check error estimates for the system. Table 1 and 2 give the observation unit vector for each camera

Table 1. Incident, observation, and system sensitivity vectors for 3 component PDV delta wing measurements in tunnel oriented and model oriented coordinate system for positions of 62.8% and 85.7% root chord.

|             | Unit Vectors<br>$k_i$ and $k_o$ (x,y,z) | System Sensitivity Vector (tunnel<br>cords.) $k_{oi}$ (x, y, z) | System Sensitivity Vector<br>(model cord) $k_{oi}$ (x', y', z') |
|-------------|---|---|---|
| Laser       | 0.009, -1.00, 0.021                     |   |   |
| Component 1 | -0.802, -0.491, 0.339                   | -0.811, 0.509, 0.318  | -0.871, 0.509, -0.024   |
| Component 2 | 0.775, -0.554, -0.304                   | 0.766, 0.446, -0.325  | 0.832, 0.446, 0.001   |
| Component 3 | -0.809, 0.48, 0.340                     | -0.817, 1.48, 0.319   | -0.877, 1.48, -0.026  |

Table 2. Incident, observation, and system sensitivity vectors for three component PDV delta wing measurements in tunnel oriented and model oriented coordinate system for positions of 97.1% and 108% root chord.

|             | Unit Vectors<br>$k_i$ and $k_o$ (x,y,z) | System Sensitivity Vector<br>(tunnel cord) $k_{oi}$ (x, y, z) | System Sensitivity Vector<br>(model cord.) $k_{oi}$ (x', y', z') |
|-------------|---|---|--|
| Laser       | 0.012, -1.00, 0.027                     |   |  |
| Component 1 | -0.829, -0.460, 0.317                   | -0.841, 0.539, 0.290  | -0.887, 0.539, -0.062  |
| Component 2 | 0.738, -0.591, -0.326                   | 0.726, 0.409, -0.353  | 0.807, 0.409, -0.041   |
| Component 3 | -0.834, 0.448, 0.322                    | -0.846, 1.45, 0.294   | -0.894, 1.45, -0.060   |

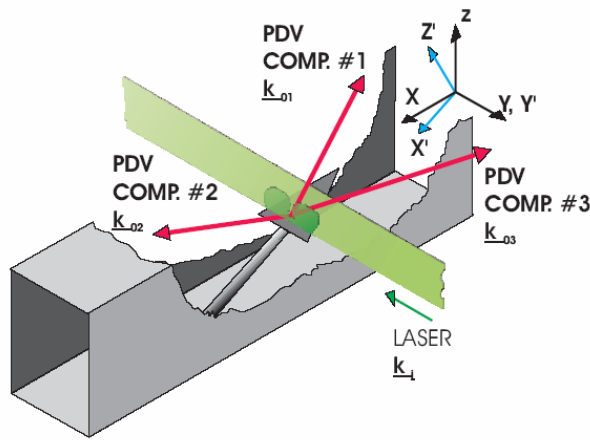


Figure 8. Camera and laser coordinate system for three component PDV test in the SARL.

velocity of approximately 69.2 m/s. PDV data was taken at four measurement locations corresponding to 62.8%, 85.7%, 97.1%, and 108% of the root-chord  $x/c$ . The light sheet was oriented perpendicular to the model surface at these locations mentioned earlier, this camera arrangement did not allow for three orthogonal velocity vectors to be derived from the data. For purposes of comparing with computational fluid dynamics, this is not a problem, since the required oblique velocity vectors corresponding to the measured velocities may be extracted from the computation. However, for viewing the velocity information, the measured components provide a combination of velocity components that leads to a non-intuitive view of the vortex velocity field. For this reason, an approximate velocity vector has been derived from the measured velocity components in the axial ( $x'$ ) and spanwise ( $y'$ ) directions as illustrated in Figure 8. These images are approximate in the sense that the velocity vectors shown were constructed on a nominal image sensitivity vector, not on a pixel-by-pixel sensitivity vector. Since there is only a weak dependence on the  $z'$  velocity components in each of these three camera systems, the axial or chordwise ( $x'$ ) and spanwise ( $y'$ ) velocities may be calculated from any two camera views with only a small residual error (approximately 4%) due to the contribution of the vertical ( $z'$ ) velocity component.

Figure 9 shows the axial ( $x'$ ) velocity calculated from the above procedure for the four axial root chord locations studied (62.8%, 85.7%, 97.1%, 108%) for the  $70^\circ$  delta wing at  $23^\circ$  angle of attack. The data in each of these images is based on an average of 200 images, with the data averaged only after it was reduced to frequency. The two vortices created above the delta wing are clearly visible where the axial velocity is greatly increased in the core of the vortex as expected. As the vortices develop downstream, the peak velocity in the core decreases and the diameter of the leading edge vortices also increases. There is some asymmetry in the vortex pair shown in the

component ( $k_{o1}$ ,  $k_{o2}$ ,  $k_{o3}$ ) and incident light unit vector ( $k_i$ ) with the system sensitivity vector  $k_{oi1}$ ,  $k_{oi2}$ ,  $k_{oi3}$  also given for each camera view for the two upstream and two downstream locations. The system sensitivity vectors are given in both tunnel ( $x, y, z$ ) coordinates and model coordinates ( $x', y', z'$ ). The laser and camera viewing angles were carefully chosen so that the views would be clear of any surface reflections from the delta wing model. These surface reflections had been observed in previous tests of the PDV system with this model, and may contaminate data. However, while the cameras and laser sheet all were arranged to view the flat delta wing model edge-on, the result was that the measured velocity components were not linearly independent. Thus, three orthogonal velocity components cannot be derived from this data set.

The tunnel was operated at Mach 0.2 for all the measurement locations resulting in a free stream

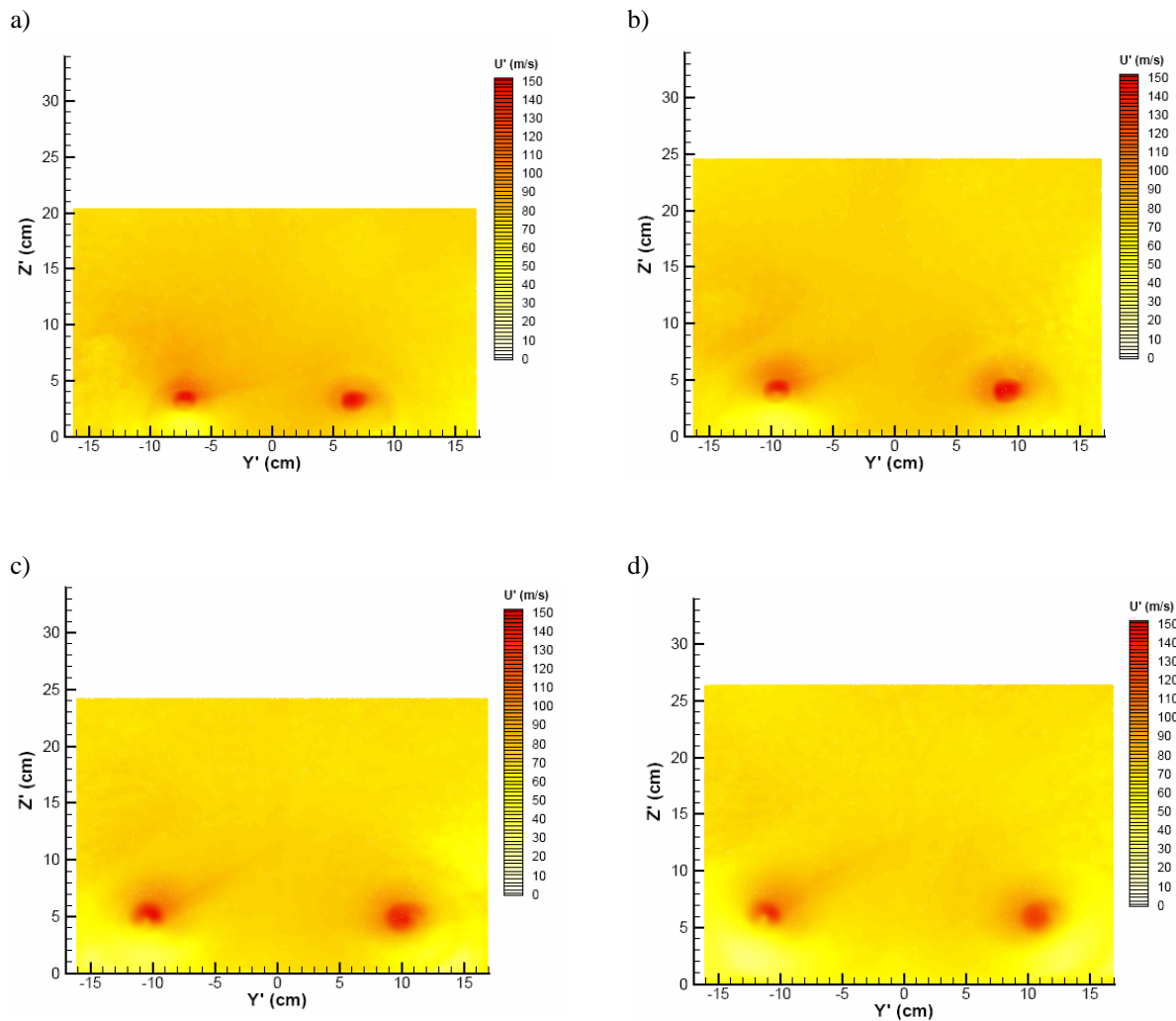


Figure 9. Axial velocity ( $X'$ ) velocity component at (a) 62.8% , (b) 85.7%, (c) 97.1%, and (d) 108 % root chord for the flow over a  $70^\circ$  delta wing at  $23^\circ$  angle of attack in a Mach 0.2 flow.

figure, with the vortex on the left side of the image showing an unusual shape. Careful examination of the image also shows a faint diagonal feature emanating from the left hand vortex and extending upward to the right. These features, while not physical features of the vortex, appear in the image due to secondary scattering effects. The wind tunnel test utilized two forms of seed particles. Theatrical fog fluid was introduced in the inlet of the wind tunnel and provided a diffuse scattering medium of small oil droplets in the flow. In addition, the ambient humidity of the air provided condensation in the vortex core that produced a much stronger scattering intensity in this region of the flow. The oblique viewing angle of the cameras captured secondary scattering off the condensation in the vortex core in the region around the left hand vortex. By contrast, the vortex on the right side was viewed more nearly orthogonally by the cameras, so that secondary scattering from the vortex core was behind the region where strong secondary scattering in the vortex core produced very strong signal strength. The errors associated with secondary scattering are most pronounced in instances such as this when a very strong scattering source, such as condensation, is present behind the light sheet in a region where the measured signal from scattering in the sheet is relatively low. In this case, the scattering in the sheet in this region was from seeding that was relatively sparse compared to the condensation.

Aside from regions in the vortex contaminated by secondary scattering, the increase in peak streamwise velocity in the vortex core is consistent with that observed in computations. Figure 10 shows a spanwise velocity cutting through the peak velocity regions of the left and right vortex cores. The velocity in the core decreases slightly (10 to

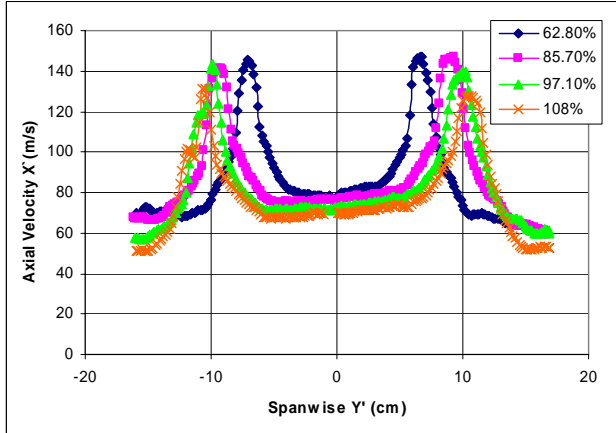


Figure 10. Axial velocity through peak velocity of vortex.

error analysis for PDV measurements, taking into account individual uncertainties of the independent variables (calibration coefficients, transmission profiles, photodiodes, camera intensity measurement, position of incident and

13%) with streamwise distance indicating that the vortex system is approaching a burst condition. Also apparent in Figure 10 is the lower velocity wake region at the 108% root chord location. Figure 11 gives the spanwise velocity component for the 70° delta wing at 23° angle-of-attack. Strong spanwise velocities are seen at the top and bottom of the vortex. The directions and magnitudes of the velocity are within the expected range, but there may be a slight bias in the lower portion of the left vortex for the reasons stated above. Again, the viewing angle provides a better measurement of the right vortex. The spanwise velocity also captures the vortex growth in diameter with streamwise distance.

The uncertainty for these measurements has been evaluated in a manner similar to previously reported

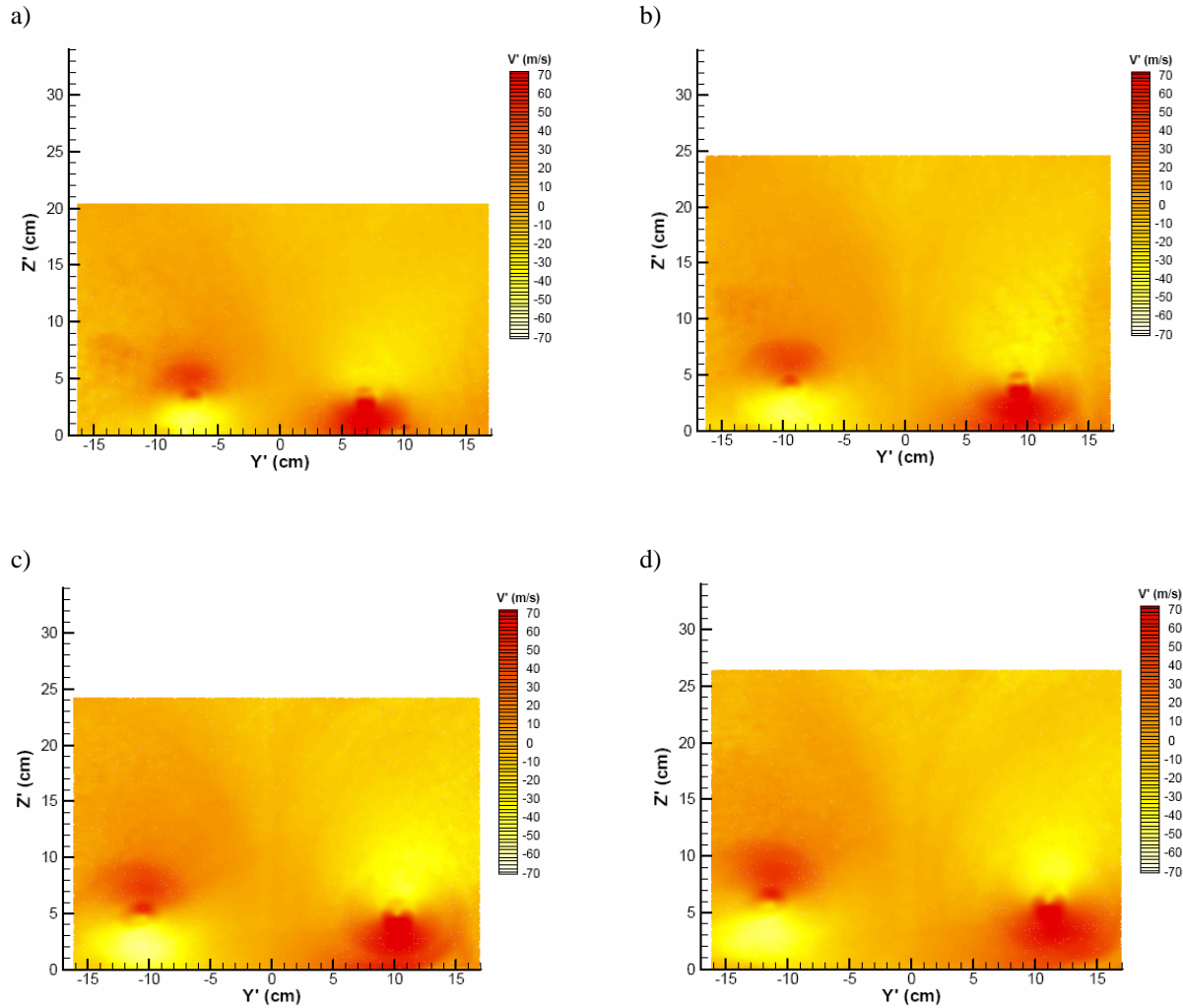


Figure 11. Spanwise velocity ( $Y'$ ) velocity component at (a) 62.8% , (b) 85.7%, (c) 97.1%, and (d) 108 % root chord for the flow over a 70° delta wing at 23° angle of attack in a Mach 0.2 flow.

observation vectors, etc.) in the system.<sup>2,24,25</sup> The uncertainty in the mean axial and spanwise velocities for the above delta wing measurements was found to be 3.4 m/s and 2.19 m/s respectively. Empty tunnel freestream velocity measurements (with the delta-wing model removed and the sting positioned away from the measurement plane) provided a check on this uncertainty calculation. Transforming the (69.2 m/s) freestream velocity into the model normal coordinate system, results in an expected axial ( $x'$ ) velocity component of 63.7 m/s. The velocity measured using PDV was 66.9 m/s which is a difference of 3.2 m/s or 5%.

### B. Boeing Unmanned Combat Air Vehicle

After initial development of PDV utilizing the relatively simple delta wing model, the system was improved and applied to measure the three component velocity field above a Boeing UCAV model illustrated in Figure 12. The UCAV model was a hybrid design and built by John Hopkins University Applied Physics Laboratory with an internal metal structure to withstand the aerodynamic loading and external shape constructed from a rapid prototype stereo lithography polymer. The model has a lambda wing planform with a span of approximately 4 feet and length of 3 feet. Control surfaces on the trailing edge could be adjusted from -20 to +20 degrees. The UCAV model been the subject of both computational simulations with an Euler solver and experimental studies including aerodynamic force and moments, pressure sensitive paint, and surface deflection using Moiré Interferometry. Other measurement results on this model are reported by Tyler.<sup>34</sup>

PDV Measurements were taken at five measurement planes (measured along the model surface relative to the wing/body junction) as shown on Figure 12. For the data presented here the trailing edge control surface was set at positive 20 degrees with the control surface deflected up. All the experiments conducted for the PDV test were at a Mach number of 0.2 (which is approximately 68 m/s for the atmospheric conditions of these experiments) and 20 degrees angle of attack measured with tunnel off conditions. The data shown is based on an average of 300 instantaneous measurements with the data averaged after it was reduced to frequency. Data for other control surface locations and comparison with computations are reported fully by Tyler<sup>35</sup> with only data demonstrating the capability of the PDV system developed shown here.

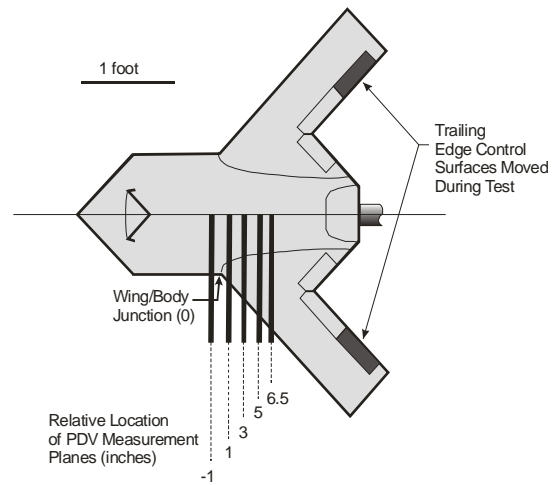


Figure 12. Schematic of Boeing UCAV model used in 3-D PDV tests.

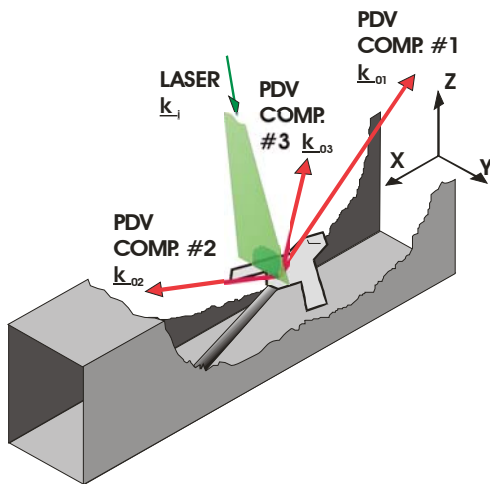


Figure 13. Camera and laser coordinate system for three component PDV Boeing UCAV test in the SARL.

Three component PDV measurements were taken with the cameras arranged as shown in Figure 13 and incident and observation vectors given in Table 3. The laser beam was introduced from the top of the tunnel. The sheet made an angle of approximately 20 degrees with respect to the free stream direction. This resulted in a sheet that was oriented normal to the model axis. Two dual camera PDV systems (as shown in Figure 5) were located on the side of the tunnel with the third PDV camera system located on the top of the tunnel. Although one would like to select camera views that result in optimized sensitivity for calculating the three tunnel oriented velocity components, the views are generally constrained to trade-offs of providing a clear view of the sheet, avoiding background reflections, and avoiding obstructions due to the model geometry. Due to the large scale of the model, semi-span measurements were taken.

Figure 14 to 18 show the 3D velocity measurements for the streamwise planes with the trailing edge control surface set at -20 degrees. In these figures, the black line on the model indicates the laser sheet position on the model surface (note the

Table 3. Incident, observation, and system sensitivity vectors for three component PDV Boeing UCAV model measurements in tunnel oriented coordinate system.

|             | Unit Vectors<br>$k_i$ and $k_o(x,y,z)$ | System Sensitivity<br>Vector (tunnel<br>cords.) $k_{oi}(x, y, z)$ |
|-------------|--|---|
| Laser       | -0.354, 0.016, -0.935                  |   |
| Component 1 | -0.726, 0.0448, 0.686                  | -0.372, 0.029, 1.62   |
| Component 2 | 0.864, -0.464, -0.194                  | 0.1.21, -0.480, 0.741   |
| Component 3 | -0.889, -0.423, 0.175                  | -0.535, -0.439, 1.11  |

vorticity sheet shed off the sharp 90 degree sweep leading edge extension. Figure 14 shows the streamwise velocity distribution in a color map and the in-plane velocity distribution as vectors on the image. The velocity distribution shows the circulation typical of the leading edge vortex. The vorticity sheet is visible on the outboard side of the vortex. Moving downstream of the wing/body junction (Figures 15 and 16) the inboard vortex has increased in diameter significantly with the streamwise velocity of the vortex core decreasing to free stream levels. A second outboard vortex created from the leading edge of the wing is visible. The outboard vortex has a significantly higher streamwise velocity in the core. Unfortunately, the presence of surface reflections does not enable the velocity near the surface to be completely resolved (i.e. the negative y component of the vortex). At the measurement plane of 5.0 inches downstream of the wing/body junction, (Figure 17) the inboard vortex continues to increase in size. At this location, the vortex has a large decrease of streamwise velocity in the vortex core. This streamwise-velocity in the core eventually goes near zero (0.8 m/s) by the last measurement location (Figure 18). The decrease in the streamwise velocity of the vortex core to zero or negative velocities is indicative of vortex bursting. As the outboard vortex develops it grows in strength and moves further outboard, but then the velocity in the vortex core decreases sharply by the last measurement location suggesting that it may also have burst.

model is shown in rendered form at its approximate location in the image). The model intersection location was measured using mapped images of the laser sheet at reduced power to avoid saturation in the image.

For the first measurement plane, located 1.0 inches upstream (Figure 14) of the wing/body junction, a vortex (which we will term the inboard vortex) is clearly visible. The inboard vortex is generated by the

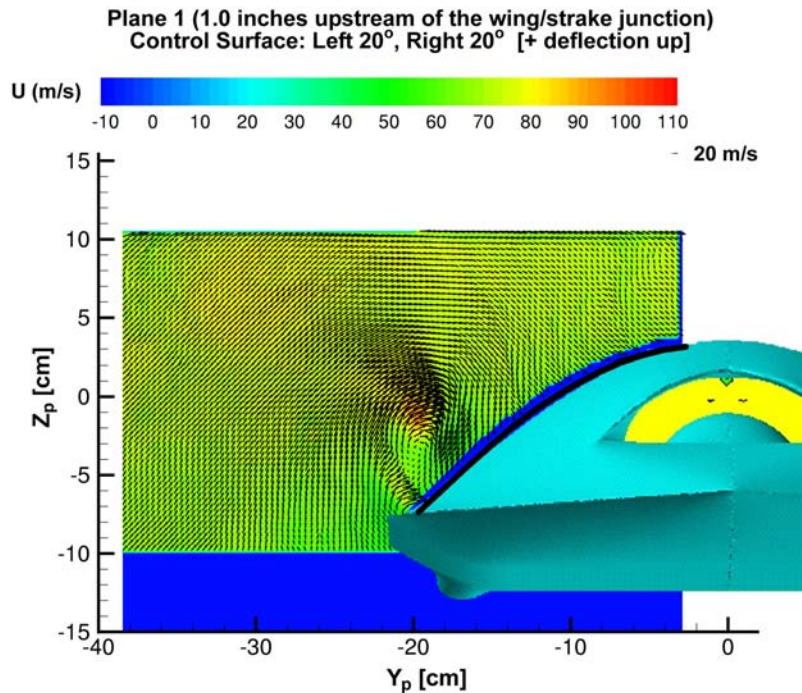


Figure 14. Three component velocity field measured using PDV of the Boeing UCAV model. The semi-span measurement plane is located at 1.0 inch upstream of the wing/body junction. The control surface deflection is 20°.

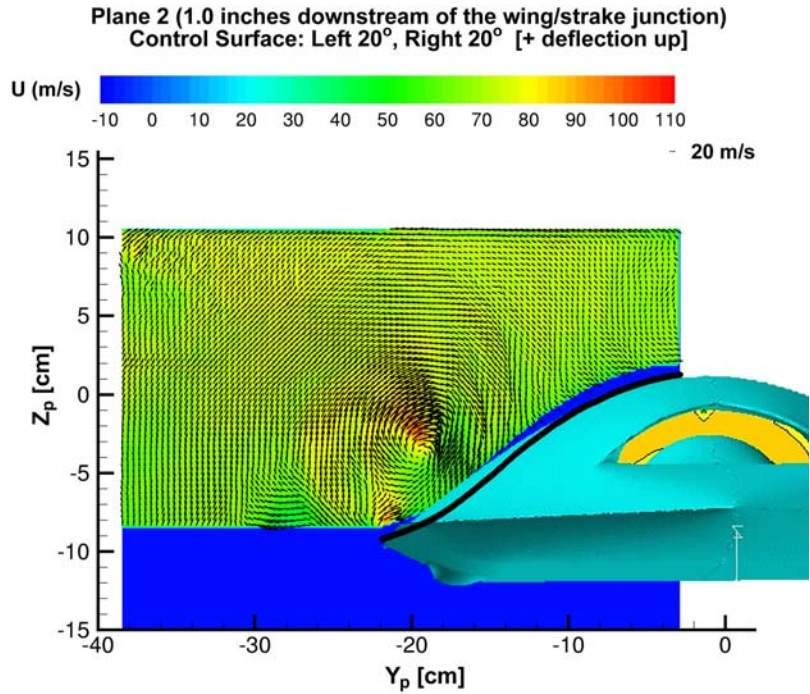


Figure 15. Three component velocity field measured using PDV of the Boeing UCAV model. The semi-span measurement plane is located at 1.0 inch downstream of the wing/body junction. The control surface deflection is 20°.

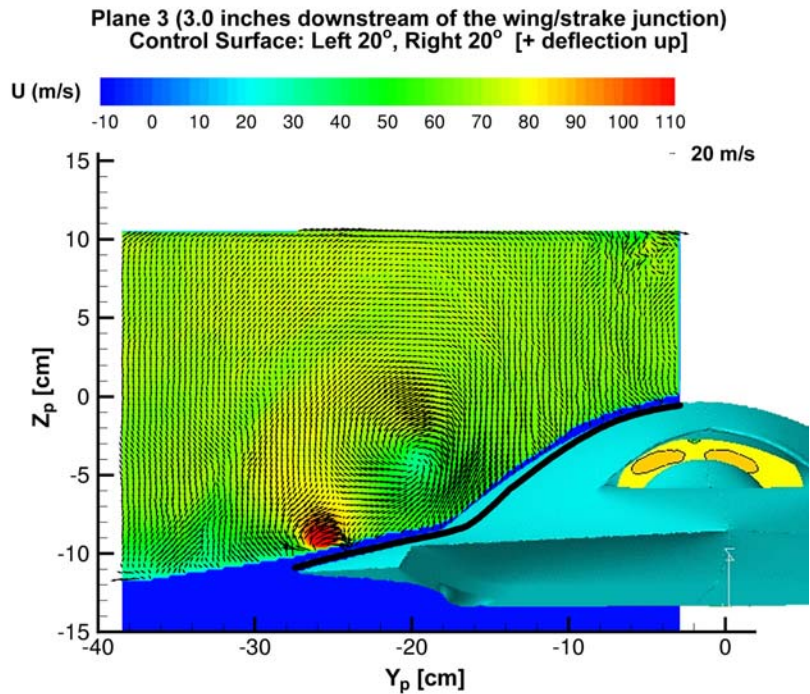


Figure 16. Three component velocity field measured using PDV of the Boeing UCAV model. The semi-span measurement plane is located at 3.0 inches downstream of the wing/body junction. The control surface deflection is 20°.

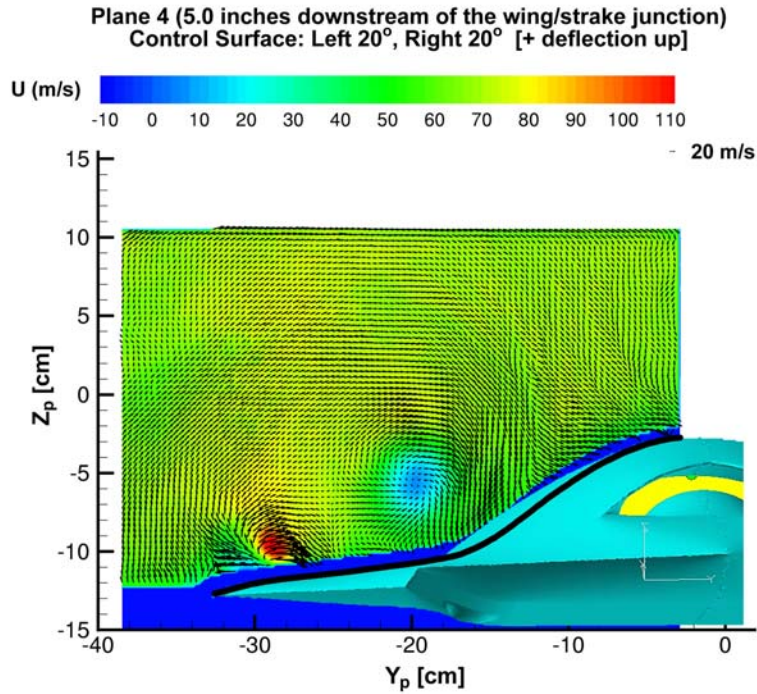


Figure 17. Three component velocity field measured using PDV of the Boeing UCAV model. The semi-span measurement plane is located at 5.0 inches downstream of the wing/body junction. The control surface deflection is 20°.

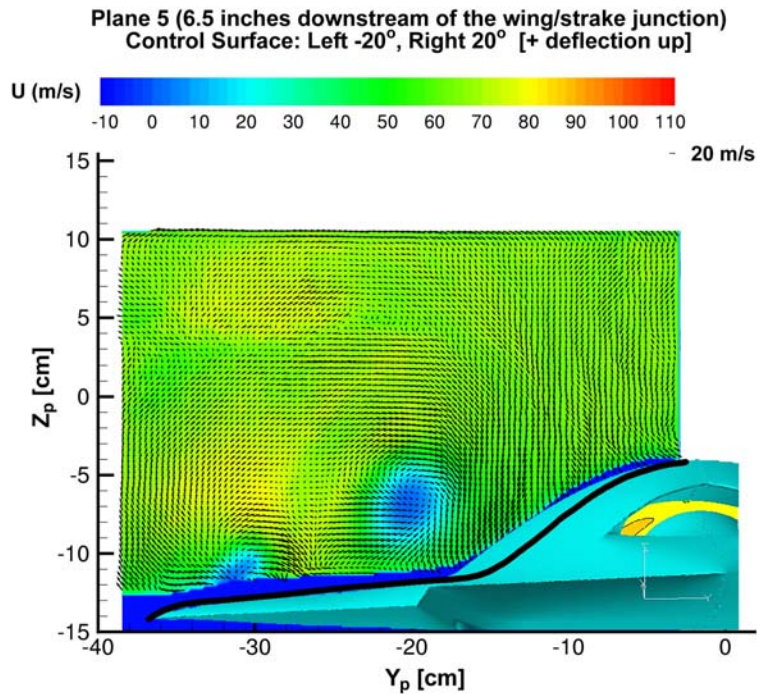


Figure 18. Three component velocity field measured using PDV of the Boeing UCAV model. The semi-span measurement plane is located at 6.5 inches downstream of the wing/body junction. The control surface deflection is 20°.

Again, uncertainty for these measurements has been evaluated in a manner similar to the previous analysis results in an uncertainty for the mean velocity of the x, y, and z components of 2.8, 6.7, and 1.9 m/s, respectively, for the UCAV measurements presented here. It should be noted that due to a failure in one of the Joulemeters during the test we were only able to scan and obtain the absorption profiles of one iodine cell at a time. Therefore the wavemeter filter had a slight shift of 10 MHz and the third camera filter component filtered had a shift from 0 to 15 MHz. This uncertainty of the filter profiles was easily calibrated using the free stream velocity of the tunnel.

### C. Considerations for Camera Viewing Angles

Many factors combine to determine the placement of cameras and laser sheet forming optics in a wind tunnel test, and hence the measured velocity components. Optical access may be limited by wind tunnel window placement, or obstructions such as wind tunnel structural supports. The window through which the laser sheet is formed may be further constrained to be higher quality glass to avoid burning the window, and a glancing impingement of the light sheet on the model surface is generally preferred to avoid damage to the model surface and the very strong reflections that arise when the light sheet directly impinges on the model surface. Finally, the region of interest on the model may constrain the viewing angles since model features such as tails, fuselage, etc. may obscure the region of interest when viewed from many angles. These constraints become particularly severe when performing 3-component velocimetry tests, since optical access and unobscured viewing must be achieved for all 3 camera systems simultaneously. These constraints may lead to undesirable viewing angles for reconstructing orthogonal velocity components, such as the test condition discussed earlier in which the set of linear equations needed to solve three velocity components for the delta wing case was found to be nearly linearly dependent. However, one can assess the quality of the viewing angles *a priori* by considering the sensitivity of the resulting uncertainty in derived velocity components (i.e. typically velocity components in orthogonal directions in either a tunnel-fixed or model-fixed reference frame) to the uncertainties in the measured velocity components (i.e. the velocity components to which each PDV camera was sensitive, given by Equation 1.)

To assess the impact of viewing angles, we first rewrite Equation 1 to reduce the number of variables in the optimization procedure and to more easily express some viewing angle constraints. For the discussion that follows, we will not consider geometric constraints introduced by optical access in the wind tunnel, or by blockage from model components. Such constraints will obviously limit the angles possible for both the incident laser sheet and the cameras. However, the procedure described will still provide an assessment of the best possible viewing angles, with additional constraints necessary based on particular tunnel and model geometries.

Figure 19 shows the coordinate system used in the analysis with the light wave vectors described in terms of three angles. Most often, it is preferred to have the plane of the laser sheet defining the measurement region oriented with the geometry of the model (i.e. normal or parallel to the model surface) or oriented in the direction of the flow coordinate system (i.e. normal or parallel to the free stream direction). For the present optimization we will assume the later condition with the light sheet oriented normal to the freestream flow direction. For a right-handed tunnel coordinate system with the x-axis in the freestream flow direction, the y-axis in the spanwise direction, and the z-axis in the vertical direction, the laser sheet will lie in the y-z plane. Defining incident and viewing angles, as shown in Figure 19, the angle  $\theta$  is the orientation of the laser direction in the y-z plane as measured from the y-axis.

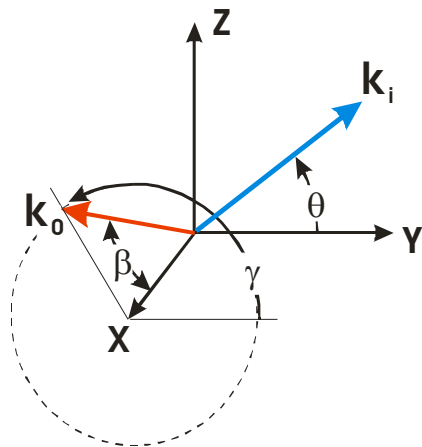


Figure 19. Coordinate system for optimization analysis of PDV positions.

Next, the observation light vector for each PDV camera component is defined by two angles:  $\beta$ , measured from the x axis, and  $\gamma$ , measured from the y axis. The possible range of  $\beta$  is from 0 to 180 degrees with the range of  $\gamma$  from -180 to 180 degrees. These viewing angle ranges describe all possible viewing angles of the laser sheet. Although there is no reason in practice to limit  $\gamma$ , one might want to limit  $\beta$  to angles between 0 and 60 degrees and 120 to 180 degrees so that the laser sheet is not viewed at too oblique an angle. Highly oblique viewing angles lead to significant optical distortion and depth of field concerns for the camera, and they may also decrease the effective resolution of the camera up to the limit of 0 or 180 degree viewing angles at which the sheet would be viewed “edge-on”. In addition, as noted in Equation 1, the sensitivity of the system depends on the viewing angle. Since the difference  $(\underline{k}_0 - \underline{k}_i)$  is not a unit vector, its magnitude may vary from a value of 0 (i.e. no sensitivity) when  $\underline{k}_0$  and  $\underline{k}_i$  are coincident (i.e.

forward scattering) to a value of 2 when  $\underline{k}_0$  and  $\underline{k}_i$  are directly opposite (i.e. backward scattering). When deciding on the camera positions, this magnitude of the sensitivity vector should be considered along with the frequency range of the absorption feature and the velocity range expected in the flow. If increased sensitivity is desired, a backward scattering direction may be used, but with the effect that a reduced velocity range will be measurable with such an arrangement.

Using  $\theta$  defined in Figure 19 the incident laser light vector ( $\underline{k}_i$ ) is given by

$$\underline{k}_i = 0\hat{i} + \cos\theta\hat{j} + \sin\theta\hat{k} \quad (8)$$

Let the subscript n denote the nth camera system component. From the two angles  $\beta_n$  and  $\gamma_n$  the observation light vector for the n<sup>th</sup> PDV component is given by

$$\underline{k}_{0n} = \cos\beta_n\hat{i} + \sin\beta_n\cos\gamma_n\hat{j} + \sin\beta_n\sin\gamma_n\hat{k} \quad (9)$$

It should be noted that in both Equation 1 and Equations 8 and 9 above, the incident and observation vectors are unit vectors with a magnitude of 1.

In addition to the considerations mentioned above, two additional figures of merit should be considered in the placement of the PDV cameras. First, as one considers the calculation of multiple components from multiple detector systems (Equation 7), we know that if the determinant of the coefficient matrix of the linear set of equations is zero the equations are linearly dependent and therefore it is not possible to solve for the individual velocity components. Therefore, one figure of merit is the condition number of the matrix, that indicates the degree to which the linear set of equations is independent. The condition number of the coefficient matrix  $\mathbf{A}$  which is defined as:

$$c = \|\mathbf{A}\| \|\mathbf{A}^{-1}\| \quad (10)$$

where  $\|\mathbf{A}\|$  is the norm of the matrix  $\mathbf{A}$ . Large values of the condition number indicate that the matrix is nearly singular and values near 1 (the minimum condition number possible for a diagonal matrix) indicate that the equations are strongly linearly independent.<sup>26, 36</sup> The condition number also provides an indication of how perturbations or uncertainties are amplified in the matrix solution. The optimum camera system placement for a three-component measurement would minimize the condition number.

The second figure of merit to consider is the minimization of uncertainty due to laser fluctuations. Clancy<sup>37</sup> proposed that the effect of laser fluctuation could be eliminated for their two-component arrangement by properly locating the detectors across from each other and evaluated the propagation of uncertainty for their camera arrangement. Here we will look at a slightly more general evaluation of the effect of the laser fluctuation and techniques to reduce system sensitivity to laser fluctuations.

A fluctuation in laser frequency has the characteristic of resulting in a frequency shift in the same direction for all components. In a three-component system with arrangement and angle definitions given previously (Figure 19 and equations 8 and 9), laser frequency fluctuations can be eliminated in two of the three velocity components. To eliminate the effect of the laser frequency fluctuation from the x and z velocity components the  $\gamma$  and  $\beta$  must be defined as

$$\begin{aligned} \gamma_1 &= \gamma & \beta_1 &= \beta \\ \gamma_2 &= -\gamma & \beta_2 &= \beta \\ \gamma_3 &= -\gamma & \beta_3 &= 180 - \beta \end{aligned} \quad (11)$$

with the integer subscripts 1, 2, and 3 indicating the three PDV components. Strictly speaking, this condition may only hold at one point in an image, since the incident light and observation direction vectors vary for each pixel in the camera array. But satisfying the above conditions for the nominal camera viewing angles will still reduce system sensitivities to laser frequency shifts. Note that  $\theta$  can be set to any direction as long as the coefficient matrix in Equation 7 is not singular. Alternatively the effect of the laser frequency fluctuation can be minimized for the x and y velocity components by defining  $\gamma$  and  $\beta$  as

$$\begin{aligned} \gamma_1 &= \gamma & \beta_1 &= \beta \\ \gamma_2 &= 180 - \gamma & \beta_2 &= \beta \\ \gamma_3 &= 180 - \gamma & \beta_3 &= 180 - \beta \end{aligned} \quad (12)$$

Thus, a recommended approach to choosing viewing angles would be: Determine the angles  $\gamma$  and  $\theta$  that minimizes the condition number for a given angle  $\beta$  where the angles  $\gamma_n$  and  $\beta_n$  are given for the n<sup>th</sup> PDV component by Equation 12.

It should be noted that from the above analysis one could construct a PDV system with four cameras in which all three velocity components could be measured with reduced sensitivity to laser frequency fluctuations. Such a system would have the further desirable property of providing a redundant velocity measurement for error

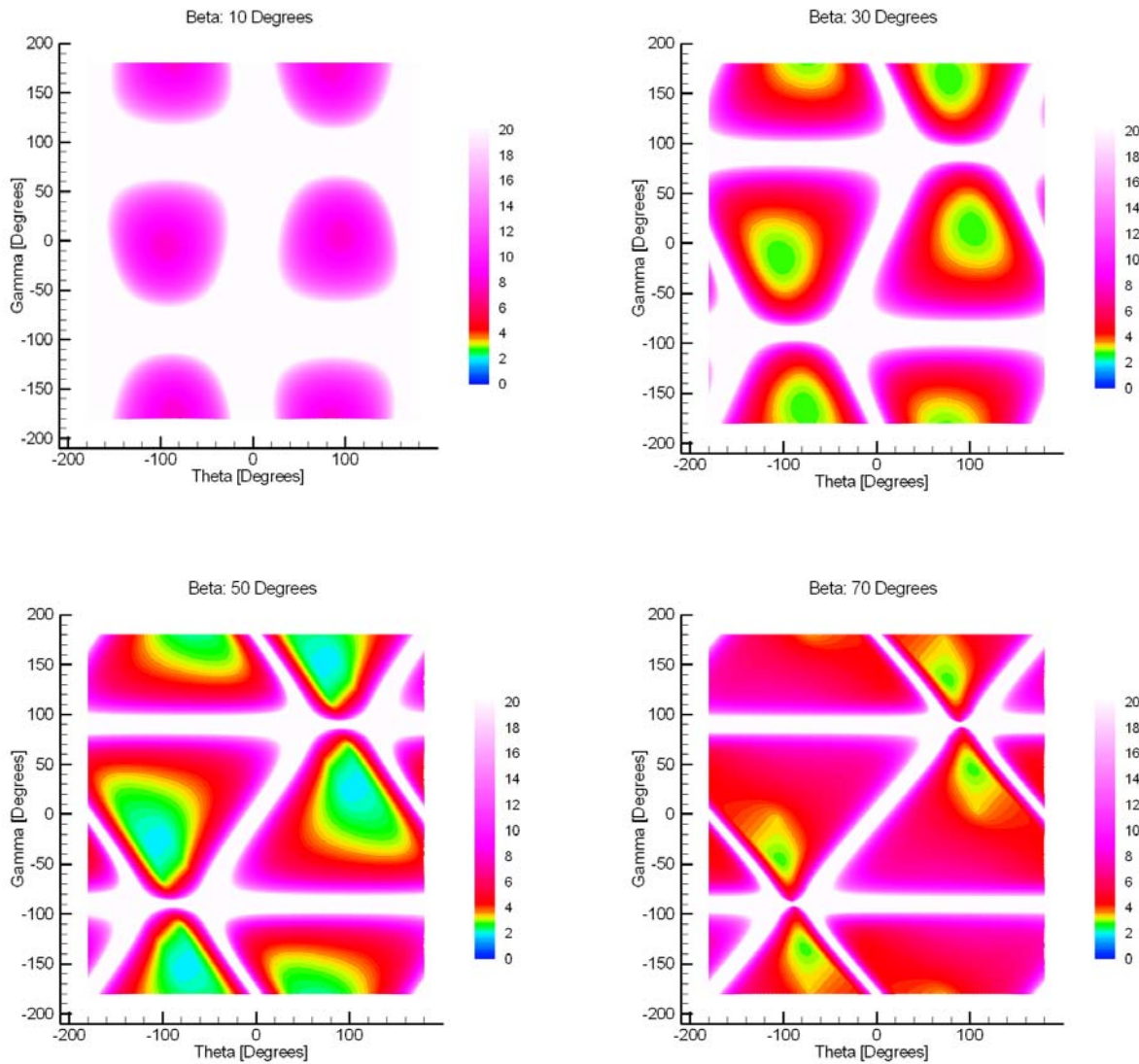


Figure 20. Optimized condition number as a function of PDV position angles ( $\beta = 10, 30, 50$  and  $70$  degrees) for optical arrangements where the effect of laser frequency fluctuations on the velocity is eliminated in the  $x$  and  $y$  directions.

estimation. Even in such a system, however, a wavemeter or other laser frequency monitoring system would be required to monitor the position of the laser frequency in the iodine transmission profile, since the laser may drift and the profile is not linear. Furthermore, the above analysis considers only nominal viewing angles, and such a system would require these conditions to be satisfied on a pixel-by-pixel basis. While the optical access constraints of most wind tunnels would make such a system impossible, such as free jet flows or atmospheric flows, the viewing angles may be more flexible. In addition, for a point measurement system, as opposed to a planar measurement system, these conditions could be more readily achieved at the measurement point. Such a system would have reduced sensitivity to laser frequency fluctuations and may be an attractive arrangement for an optical air data probe.

Figure 20 shows the contours of the condition number as a function of  $\gamma$  and  $\theta$  for given  $\beta$  which ranges from 10 degrees (where the PDV components are observing the laser sheet almost normally) to 70 degrees (where the PDV components are relatively oblique to the laser sheet making them impractical for imaging measurements). As can be observed the condition number has four minima with two each in the first and third quadrants. The angle  $\beta$  for the

Table 4. Incident light and observation vectors for optimized position according to condition number with no uncertainty due to laser fluctuations on x and y components.

|             | Unit Vectors<br>$k_i$ and $k_o(x,y,z)$ | System Sensitivity<br>Vector (tunnel coord.)<br>$k_{oi}(x, y, z)$ |
|-------------|--|---|
| Laser       | 0.00, -0.174, 0.985                    |   |
| Component 1 | 0.643, 0.705, 0.299                    | 0.643, 0.879, -0.686  |
| Component 2 | 0.643, -0.705, 0.299                   | 0.643, -0.531, -0.686   |
| Component 3 | -0.643, -0.705, 0.299                  | -0.643, -0.531, -0.686  |

condition number at any  $\beta$ . This is shown in Figure 21. Since there is symmetry in the solution we have constrained the problem to the first quadrant with  $\gamma$  between 0 and 90 degrees and  $\theta$  constrained between 0 and 180 degrees. As observed for a range of  $\beta$ , the condition number is always less than 8, which is still a well conditioned set of viewing angles. The optimal condition number is 1.93 which occurs for angles of  $\gamma = 23^\circ$ ,  $\theta = 100^\circ$  and  $\beta = 50^\circ$ . Table 4 gives the observation and incident light vectors for this arrangement. This arrangement would be possible in many wind tunnel and jet studies where the major free stream flow direction was oriented along the x-axis allowing the cameras to be mounted outside the tunnel and away from the flow, however in many cases, the model geometry itself—tails, fuselage—may obscure one or more viewing angle for a region of interest and prevent this optimal set of viewing angles.

Table 5 gives the determinant and condition number for the PDV data presented in this paper for the delta wing and UCAV. As shown in the table, the condition number for the delta wing experiment is very high (217 and 58) for the case where all three camera systems are used to calculate three velocity components (indicating that the equations are linearly dependent and can not be used to solve three velocity components). However the two-component delta wing data has a relatively low condition number (4.15 and 4.0) so that the two velocity components in model normal coordinates can be accurately resolved. For the UCAV test, the condition number is again relatively low (5.14) which results in the ability to resolve and measure all three velocity components for this flow field.

minimum condition number occurs at an angle of 50 degrees, where the condition number reaches a minimum of 1.93. These plots indicate the optimized position to arrange the cameras to eliminate laser fluctuation of two components of velocity while minimizing the uncertainty of the measurement of multiple components for the angles  $\gamma$ ,  $\theta$ , and  $\beta$ . For a case where practical optical constraints (i.e. the location of windows, or the direction of the free stream) are not an issue, we can plot the angles  $\gamma$ ,  $\theta$ , for minimum

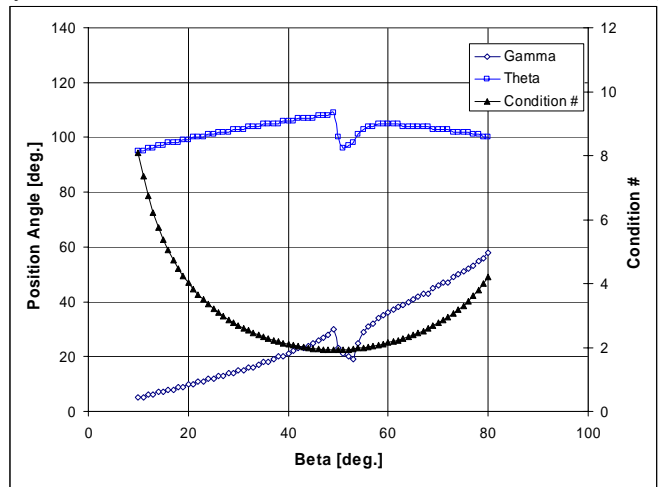


Figure 21. Optimized condition number and position angles gamma and theta for any angle beta for the PDV set-up as described.

Table 5. Determinant and Condition Numbers for PDV UCAV Measurements.

| Data Set                                     | Determinant | Condition # |
|--|-------------|-------------|
| 3D – Delta Wing<br>62.8% & 85.7% root chord  | -0.018      | 217.3       |
| 3D – Delta Wing<br>97.1% and 108% root chord | -0.063      | 58.2        |
| 2D – Delta Wing<br>62.8% & 85.7% root chord  | 0.86        | 4.2         |
| 2D – Delta Wing<br>97.1% and 108% root chord | 0.84        | 4.0         |
| 3D – Boeing UCAV                             | -1.26       | 5.14        |
| 3D – Optimized configuration                 | 1.24        | 1.93        |

The analysis above and the data in Table 5 are based on a nominal viewing angle typically the center of the field of view for the camera. It should be noted that the viewing angle actually changes over the camera field of view, and this must be accounted for when processing images and assessing the sensitivity to viewing angles, as each pixel in the camera is sensitive to a slightly different velocity component. This effect increases as the focal length for the camera system is decreased.

## VI. Conclusions

A Planar Doppler Velocimetry (PDV) system has been presented which is capable of measuring two or three velocity components in a plane in large subsonic wind tunnel facilities. The PDV system was demonstrated on two models; two velocity component measurements on a 70 degree delta wing, and three velocity components measured in the flow field created by a Boeing UCAV model. The velocity fields of vortices created in both flows were resolved including indications of vortex bursting for the UCAV model as the vortex developed. The uncertainty in the mean velocity measurements for the x, y, and z components calculated to be 2.8, 6.7, and 1.9 m/s respectively. Also a methodology for eliminating the effect of laser frequency fluctuations for three component measurements was presented, as well as a procedure to optimize the positions of the incident laser sheet and observation directions of the PDV cameras so that the coefficient matrix used to calculate the velocity components is as well conditioned as possible.

## Acknowledgements

This work was supported in part by a Small Business Innovative Research (SBIR) program with Innovative Scientific Solutions Inc. and the Air Force Research Laboratory, WPAFB, Ohio.

## References

- <sup>1</sup> R.L. McKenzie, "Measurement capabilities of planar Doppler velocimetry using pulsed lasers," *Applied Optics*, 35: 948-964, 1996.
- <sup>2</sup> A. Mosedale, G.S. Elliott, C.D. Carter, and T.J. Beutner, "Planar Doppler velocimetry in a large-scale facility," *AIAA Journal*, 38: 1010-1024, 2000.
- <sup>3</sup> P. Clancy, M. Samimy, and W. Erskine, "Planar Doppler velocimetry: Three-component velocimetry in supersonic jets," *AIAA Journal*, 37: 700-707, 1999.
- <sup>4</sup> B. Thurow, N. Jiang, W. Lempert, and M. Samimy, "MHZ rate planar Doppler velocimetry in supersonic jets," AIAA Paper 2004-0023, 2004.
- <sup>5</sup> M. Samimy, and M. Wernet, "A review of planar multiple-component velocimetry in high speed flows," *AIAA Journal*, 1999.
- <sup>6</sup> H. Komine, and S.J. Brosnan, "Instantaneous, three-component, Doppler global velocimetry," *Laser Anemometry*, 1: 273-277, 1991.
- <sup>7</sup> J.F. Meyers, and H. Komine, "Doppler global velocimetry: a new way to look at velocity," *Laser Anemometry*, 1: 289-296, 1991.
- <sup>8</sup> J. Kuhlman, S. Naylor, K. James, S. Ramanath, "Accuracy study of a 2-component point Doppler velocimeter. AIAA Paper 98-2607, 1998.
- <sup>9</sup> S.J. Beresh, S.P. Kearney, C.J. Bourdon, and T.W. Grasser, "Development of a Doppler global velocimeter for high-overexpanded supersonic jet," AIAA Paper 2003-0915, 2003.
- <sup>10</sup> R.W. Ainsworth, S.J. Thorpe, and R.J. Manners, "A new approach to flow-field measurement – A view of Doppler global velocimetry techniques," *International Journal of Heat and Fluid Flow*, 18: 116-130, 1997.
- <sup>11</sup> G.S. Elliott, "The study of compressible free shear layers using laser based diagnostic techniques," PhD Dissertation, The Ohio State University, Columbus, 1993.
- <sup>12</sup> G.S. Elliott, M. Samimy, and S.A. Arnette, "A Molecular Filter Based Velocimetry Technique for High Speed Flows," *Experiments in Fluids*, 18: 107-118, 1994.
- <sup>13</sup> M.W. Smith, G.B. Northam, and J.P. Dummond, "Application of absorption filter planar Doppler velocimetry to sonic and supersonic jets," *AIAA Journal*, 34: 434-441, 1996.
- <sup>14</sup> R.B. Miles, and W.R. Lempert, "Flow diagnostics in unseeded air," AIAA Paper 90-0624, 1990.
- <sup>15</sup> Forkey JN, Finkelstein ND, Lempert WR, Miles RB. Demonstration and characterization of filtered Rayleigh scattering for planar velocity measurements. *AIAA J* 1996;34:442-448.
- <sup>16</sup> Elliott GS, Glumac N, Carter CD. Molecular filtered Rayleigh scattering applied to combustion. *Meas Sci Tech* 2001;12(4):452-466.
- <sup>17</sup> Kearney SP, Beresh SJ, Grasser TW, Schefer RW, Schrader PE, Farrow RL. A filtered Rayleigh scattering apparatus for gas-phase and combustion temperature imaging. Paper 2003-0584, AIAA, January 2003.

- 
- <sup>18</sup> Boguszko, M., and Elliott, G.S., "On the use of Filtered Rayleigh Scattering for Measurements in Compressible Flows and Thermal Fields," Accepted to Experiments in Fluids, September, 2004.
- <sup>19</sup> H. Komine, S.J. Brosnan, and A.B. Litton, "Stappaerts EA. Real-time, Doppler global velocimetry," AIAA Paper 91-0337, 1991.
- <sup>20</sup> J.F. Meyers, and H. Komine, "Doppler global velocimetry: a new way to look at velocity," *Laser Anemometry*, 1: 289-296, 1991.
- <sup>21</sup> G.S. Elliott, and T.J. Beutner, "Molecular filter based planar Doppler velocimetry," Invited article for *Progress in Aerospace Sciences*, 35: 799-845, 1999.
- <sup>22</sup> J.F. Meyers, J.W. Lee, M.T. Fletcher, and B.W. South, "Hardening Doppler global velocimetry systems for large wind tunnel applications, AIAA Paper 98-2606, 1998.
- <sup>23</sup> I. Roehle, and C.E. Willert, "Extension of Doppler global velocimetry to periodic flows," *Measurement Science and Technology*, 12: 420-431, 2001.
- <sup>24</sup> J. Crafton, C.D. Carter, and G.S. Elliott, "Three-component phase-averaged velocity measurements of an optically perturbed supersonic jet using multi-component planar Doppler velocimetry," *Measurement Science and Technology*, 12: 409-419, 2001.
- <sup>25</sup> T. Beutner, G. Elliott, G. Williams, H. Baust, J. Crafton, and C.D. Carter, "Forebody and leading edge vortex measurements using planar Doppler velocimetry," *Measurement Science and Technology*, 12: 378-394, 2001.
- <sup>26</sup> Spectra-Physics, "Pulsed Nd:YAG Lasers User's Manual GCR Series," 1996.
- <sup>27</sup> Spectra-Physics, "Model 6350 Instruction Manual," 1994.
- <sup>28</sup> P. Clancy and M. Samimy, "Two-component planar Doppler velocimetry in high speed flows," *AIAA Journal*, 35:1729-1738, 1997.
- <sup>29</sup> J. Forkey, N. Finkelstein, W. Lempert, and R. Miles, "Control of experimental uncertainties in filtered Rayleigh scattering measurements," AIAA 95-0298, 1995.
- <sup>30</sup> J. Crafton, "Iodine Vapor Cell," Innovative Scientific Solutions, Inc., URL: [http://www.innssi.com/iodine\\_cell.htm](http://www.innssi.com/iodine_cell.htm) [cited 22 December 2004].
- <sup>31</sup> Stanford Research Systems, "Fast Gated Integrators and Boxcar Averagers," 1993.
- <sup>32</sup> PixelVision "User's Manual SpectraVideo Camera," 1996.
- <sup>33</sup> J. Crafton, G. Elliott, C. Carter, T. Beutner, H. Baust, and A. Mosedale, "Filtered Rayleigh Scattering Velocimetry for Wind Tunnel Applications," AFRL-VA-WP-TR-2004-3080, 2004.
- <sup>34</sup> C. Tyler, "A Joint Computational Fluid Dynamics and Experimental Fluid Dynamics Test Program," AIAA Paper 2004-, 2004.
- <sup>35</sup> C. Tyler, H. Baust, G. Elliott, J. Crafton "Multiple Computational Simulations Performed for Comparison with Planar Doppler Velocimetry Measurements," paper submitted to the 2005 AIAA Aerospace Sciences Meeting and Exhibit.
- <sup>36</sup> G. Strang, "Linear algebra and its applications," Harcourt Brace Jovanovich Inc., Orlando, Florida, 1988.
- <sup>37</sup> P.S. Clancy, "Development and application of three-component planar Doppler velocimetry for high speed flows," Ph.D. Dissertation, The Ohio State University, Columbus, 1997.